Soft Matter

Accepted Manuscript

This is an *Accepted Manuscript*, which has been through the Royal Society of Chemistry peer review process and has been accepted for publication.

Accepted Manuscripts are published online shortly after acceptance, before technical editing, formatting and proof reading. Using this free service, authors can make their results available to the community, in citable form, before we publish the edited article. We will replace this *Accepted Manuscript* with the edited and formatted *Advance Article* as soon as it is available.

You can find more information about *Accepted Manuscripts* in the Information for Authors.

Please note that technical editing may introduce minor changes to the text and/or graphics, which may alter content. The journal's standard Terms & Conditions and the Ethical guidelines still apply. In no event shall the Royal Society of Chemistry be held responsible for any errors or omissions in this *Accepted Manuscript* or any consequences arising from the use of any information it contains.

ROYAL SOCIETY OF CHEMISTRY

www.rsc.org/softmatter

ARTICLE TYPE www. rsc.org/xxxxxx | XXXXXXXX

Fluorinated lamellar phases: structural characterisation and use as templates for highly ordered silica materials†

Matthew J. Pottage,[a] Tiara Kusuma,[b] Isabelle Grillo,[c] Christopher J. Garvey,[d] Anthony D. Stickland[b] and Rico F. Tabor*[a]

Received Xth XXXXXXXXXX 20XX, Accepted Xth XXXXXXXXX 20XX
First published on the web Xth XXXXXXXXXX 200X
DOI: 10.1039/b000000x

Highly ordered silica was synthesised by using a lamellar phase comprising the anionic fluorinated surfactant sodium perfluorooctanoate and the partially-fluorinated co-surfactant/oil 1H,1H,2H,2H-perfluorooctan-1-ol in water. The phase behaviour of this system was thoroughly analysed, and it was found that even low levels of the alcohol (<0.5 mol %) were sufficient to induce a phase change from normal micelles to a lamellar phase, rationalised as a result of geometric and electrostatic effects. The properties of these phases were compared to their hydrocarbon analogues, demonstrating the unique and valuable properties exhibited by fluorocarbons, directly related with the observed nanostructure. Small-angle neutron scattering was used to analyse the internal structure of the systems, providing information on the inter-lamellar spacing, bilayer thickness and membrane elasticity. The potential for these phases to act as shear-thinning lubricants was assessed using oscillatory rheology, obtaining shear-dependent viscosity along with storage and loss moduli.

Introduction

Fluorinated amphiphiles have generated a great deal of interest over recent decades due to many unusual properties when compared with their hydrocarbon counterparts[1]. The strength of fluorine-carbon bonds coupled with the much larger volume of fluorine atoms compared to hydrogen makes fluorocarbon chains rigid, robust and thermally stable with low dispersion forces; they are also dense, extremely hydrophobic and tend to have significantly lower water solubility than hydrocarbon analogues[2]. These properties make them attractive surfactants for coatings, foams, dispersions and electronic applications[1]. In addition, their often advantageous demixing from hydrocarbons[3] has made them of great interest in polymer chemistry[4] and particle synthesis[5]. However, these same properties also present some significant disadvantages to their use: they tend to be more challenging and expensive to synthesise[6] and extremely environmentally persistent[7] (as strikingly few microorganisms can digest them), making control of their usage and disposal an important consideration. Thus, the fundamental exploration of the physical basis *why* fluorinated materials exhibit their unique and useful properties is important, such that we can design environmentally-benign alternatives with the same characteristics.

Previous studies of the properties of fluorinated amphiphiles have found a greater propensity to form low curvature phases such as lamellar phases and vesicles than their hydrocarbon counterparts[8–10], rationalised by the larger packing volume of the rigid fluorocarbon chain. The fluorooctanoate anion readily forms lamellar phases in water when coupled with lithium[9], caesium[11] and ammonium[12] counterions. Curiously, lamellar phases are not seen for the sodium salt in water, which forms normal micelles with increasing concentration before arriving at a solid/micellar phase separation[13,14]. Such counterion-specific effects on surfactant aggregation and phase behaviour are well-documented in the literature,[15,16] including for some fluorosurfactants.[17]

Lamellar liquid crystals are excellent candidates for a range of applications including electro-optical devices, lubricants, delivery vectors and stabilisation and deployment of particles. Of particular interest for fluorinated analogues are their portential use for lubrication[18] in critical components, as they are robust and shear-thinning over a wide range of shear rates and temperatures[19].

[a] *School of Chemistry, Monash University, Clayton, VIC 3800, Australia. Fax: +61 3 9905 4597; Tel: +61 3 9905 4558; E-mail: rico.tabor@monash.edu*
[b] *Particulate Fluids Processing Centre, Department of Chemical and Biomolecular Engineering, The University of Melbourne, Parkville 3010, Australia.*
[c] *Institut Max Von Laue Paul Langevin, F-38042 Grenoble, France.*
[d] *Bragg Institute, Australian Nuclear Science and Technology Organisation, Lucas Heights, NSW 2234, Australia.*
† Electronic Supplementary Information (ESI) available: Details of SANS fitting of mixed phase samples. See DOI: 10.1039/b000000x/

In this work, we explore the phase behaviour and properties of a novel ternary system comprising the ubiquitous fluorinated amphiphile sodium perfluorooctanoate, a partially fluorinated alcohol and water. The structural characteristics are obtained by comparing neutron scattering data with rheological measurements, showing remarkable control over phase viscosity and relaxation using compositional parameters. The potential for using such phases as a template to synthesize highly-ordered silica is demonstrated. Throughout we are mindful to explore the properties of the fluorinated amphiphiles that result in their phase behaviour and rheological characteristics, in order to provide the first step toward designing their replacements.

Materials and methods

Materials: Sodium perfluorooctanoate was prepared from perfluorooctanoic acid (99%, Fluorochem, UK) by stoichiometric neutralisation in water with sodium hydroxide solution (ChemSupply, reagent grade). The co-surfactant/oil 1H,1H,2H,2H-perfluorooctan-1-ol (PFOH, 99%) was obtained from Fluorochem and used as received, and water was obtained from a Millipore Direct-Q 5, with a minimal resistivity of 18.4 MΩ·cm. For neutron scattering experiments, D_2O was obtained from Sigma (99.98 atom% D) and used as received. Templated silica was prepared using tetraethylorthosilicate (TEOS, Sigma, 99%, used as recieved) as a silicate precursor.

Phase behaviour: Samples were initially prepared as NaPFO/PFOH mixtures with varying mass ratios (0:1, 0.05:0.95, 0.1:0.9, *etc.*), and then diluted toward the water corner of the ternary phase diagram. At each stage, thermal equilibration was achieved by leaving for a minimum of 30 minutes in a recirculating water bath at 25 ± 0.05°C. Preliminary phase characteristics were assessed using visual inspection and polarising optical microscopy. Further samples were prepared close to apparent phase boundaries in order to provide more accurate delineation of phase separation regions. On the basis of tentative phase boundaries thus determined, selected points were fully characterised using small-angle neutron scattering (see below and Table 1).

Small-angle neutron scattering (SANS): SANS measurements were made on two instruments: D11 (Institut Laue-Langevin, Grenoble, France) and Quokka (ANSTO, Lucas Heights, Australia) at sample temperature of 25°C. Data are presented as a function of the scattering vector, q:

$$q = \frac{4\pi}{\lambda} \sin \frac{\theta}{2} \tag{1}$$

where λ is the incident neutron wavelength and θ is the scattering angle. The effective q range obtained for a given experiment is therefore defined by the sample-detector distance and the detector size. For D11, scattering was measured for each sample at two different configurations with sample-detector distances of 1.2 and 8 m, λ = 10 Å (with a wavelength spread defined by $\Delta\lambda/\lambda = 9\%$), and a detector offset to provide a q-range of 0.003-0.387 Å^{-1}. Similarly on Quokka, two sample-detector distances of 2 and 14 m were used with an incident wavelength of λ = 5 Å ($\Delta\lambda/\lambda = 10\%$), providing a q-range of 0.005-0.400 Å^{-1}. For each instrument, data was reduced from raw counts on the 2D detector to a radially-averaged 1D scattering pattern with the assumption of radially isotropic scattering. The sensitivity of each detector pixel was calibrated by comparison of its response to a flat scatterer, and then the scattering from an empty SANS cell was subtracted. The scattering was then radially averaged (accounting for instrument configuration) to provide the intensity as a function of q. The absolute intensity scale was provided by normalising each sample by its thickness (1 or 2 mm), and then comparing to either the scattering from a 1 mm sample of H_2O (for D11), or an empty beam measurement (for Quokka). Furthers details of the D11 and Quokka may be found on the instrument webpages.*

SANS data were fit using one of two models: for spherical micelles, a simple spherical form factor[20], $P(q)$ was used:

$$P(q) = \left[\frac{3(\sin(qr) - qr \cdot \cos(qr))}{(qr)^3}\right]^2 \tag{2}$$

where r is the particle radius. To account for the micelle polydispersity, a Schulz function was applied to the radius to obtain the distribution of radii, σ/r_{av} as a function of the width parameter, z:

$$\sigma = \frac{r_{av}}{(z+1)^{1/2}} \tag{3}$$

where r_{av} is the average radius. The structure factor used was the Hayter-Penfold construction[21] for inter-particle interactions in charged systems (a mean square approximation closure of the Ornstein-Zernicke equation).

For lamellar systems, the construction of Nallet *et al.* was applied[22]. This model comprises a form factor representing the extended lamellar sheets, $P(q)$, a structure factor that defines their interaction, $S(q)$ rationalised by the average inter-lamellar spacing, d:

$$I(q) = 2\pi \frac{P(q)S(q)}{dq^2} \tag{4}$$

* Quokka: http://www.ansto.gov.au/ResearchHub/Bragg/Facilities/Instruments/Quokka/; D11: http://www.ill.eu/instruments-support/instruments-groups/instruments/d11/

The form factor representing the lamellar 'sheets' is given by:

$$P(q) = \frac{2\Delta\rho^2}{q^2}\left(1-\cos(q\delta)\exp(-q^2\sigma^2/2)\right) \quad (5)$$

where $\Delta\rho$ is the difference in scattering length density between the bilayer and solvent, δ is the thickness of the bilayer, and σ is a parameter arbitrarily fixed at $\sigma = \delta/4$.
The structure factor representing the interactions between lamellae in the system is given by:

$$S(q) = 1+2\sum_{1}^{N-1}\left(1-\frac{n}{N}\right)\cos(qdn)\exp\left(-\frac{2q^2d^2\alpha(n)}{2}\right) \quad (6)$$

where N is the number of lamellar plates and n refers to the 'n'th layer and α is given by:

$$\alpha(n) = \frac{\eta_{cp}}{4\pi^2}\left[\ln(\pi n)+\gamma_E\right] \quad (7)$$

where γ_E is Euler's constant. The Caillé parameter[23], η_{cp} is

$$\eta_{cp} = \frac{q_0^2 k_B T}{8\pi\sqrt{K\bar{B}}} \quad (8)$$

where q_0 is the scattering vector of the first Bragg peak, k_B and T are the Boltzmann constant and the temperature respectively, K is the membrane bending elasticity and $\bar{B}$ is the membrane compression modulus.
Powder diffraction: Powder diffraction spectra were obtained using a Brüker D8 'Advance' powder diffractometer, operating at a wavelength of 1.54 Å, driven at 0.5°/min.
Polarising light miscroscopy: Polarising light microscopy (PLM) images were obtained using a CCD camera (Flea3, Point Grey, Richmond, BC, Canada) coupled to a Kozo XJP-300 polarising microscope.
Rheology: Rheological experiments were performed using a cone-and-plate geometry ($d = 40$ mm, $\theta = 2°$) in a stress-controlled rheometer (AR-G2, TA Instruments). The tests were performed in a closed environment with a small pool of water nearby to ensure high humidity and limited sample evaporation. Samples were loaded carefully to minimise air bubbles in the thickest samples, and were allowed to rest for 5 minutes prior to testing in order to minimise pre-shear history. Small Angle Oscillatory Shear (SAOS) tests were performed in which a sinusoidal stress was applied and the resulting deformation measured. Initial tests at a fixed frequency (either 0.1 or 10 Hz) with varying peak stress were used to determine the linear viscoelastic region. Subsequent frequency sweeps at stresses in the linear region were used to give the viscous and elastic moduli as functions of frequency. The frequencies ranged from 10^{-3} to 30 Hz, but varied for individual samples due to the limitations of the rheometer and the geometry. The temperature was controlled at 21 ± 0.1°C throughout the rheological tests.
Atomic force microscopy: Atomic force microscopy (AFM) images were made in tapping mode using a JPK Nanowizard 3 AFM. This instrument is equipped with capacitative sensors to ensure accurate reporting of height, z, and $x-y$ lateral distances. Cantilevers used were Brüker NCHV model tapping mode levers, with nominal resonant frequencies of 340 kHz and spring constants of 20-80 N/m respectively. Imaging was performed with a set-point force of <1 nN. Sectional heights were measured by taking line profiles (effectively a single x-z fast-axis scan line from an image). Repeated imaging at different scan angles was performed to ensure that no sample damage or artefaction affected the obtained images.

Results and discussion

Phase behaviour

Mixtures of sodium perfluorooctanoate (NaPFO), 1H,1H,2H,2H-perfluorooctan-1-ol (PFOH) and water were prepared in order to determine the ternary phase behaviour of the three components. In line with expectation from literature reports[14,24,25], NaPFO in water formed an isotropic micellar solution up to the limit of solubility. These micelles have been characterised by scattering as spherical in nature. However, addition of even low levels of PFOH resulted in the transformation of the inviscid micellar solution to a highly viscous, birefringent gel.

At higher surfactant and co-surfactant loading, the gel increased in opacity to being completely opaque. While the opacity indicates phase separation occurs over a large area of the phase space, the high viscosity prevents separation into discrete layers except for samples with high mass fraction of water. Thus, from even low loadings of co-surfactant, many of the samples outside monophasic regions are 'kinetically trapped' (unable to reach their thermodynamically stable, phase separated state due to the high sample viscosity) and clearly defining phase boundaries using visual observation alone was not possible.

By using polarising optical microscopy, more information on the nature of the phases formed was obtained (Fig. 1). At low levels of added PFOH (Fig. 1a), small 'maltese crosses' were visible, characteristic of the presence of a lamellar phase. As the concentration of PFOH increased, these crosses grew in size, suggesting larger and more ordered lamellar domains (Fig. 1b). At high levels of PFOH, this structure became disrupted, and the lamellar domains appeared to be interspered with other birefringent material, in the form of either another

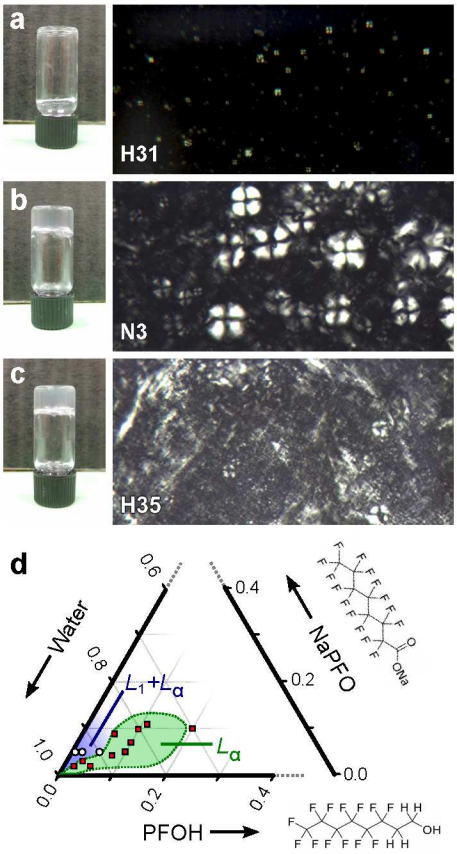

Fig. 1 a-c) Visual appearance of macroscopic samples and microscopic optical texture between crossed polarisers of characteristic NaPFO/PFOH phases at low (a), moderate (b) and high (c) concentration. The exact compositions are detailed in Table 1. d) Partial ternary phase diagram of NaPFO, PFOH and water, plotted as mass fractions. Phase boundaries were determined as described in the text, by visual and microscopic evaluation of *ca.* 200 samples. The symbols represent samples used in SANS measurements and determined to be $L_1 + L_\alpha$ (○) and pure L_α (□).

coexistent liquid crystalline phase or solid crystallites. In either case, we interpret this transition as marking the upper concentration limit of the single-component lamellar region of the phase diagram.

The experimentally determined phase diagram for the NaPFO, PFOH and water system is shown in Fig. 1. The insolubility of the ionic surfactant in the non-polar alcohol resulted in only a small area of homogenous lamellar phase in the water-rich region of the phase diagram. This lamellar phase forms even at a very low surfactant and oil loadings, which is unusual for a soft matter system composed of small amphiphiles (such as the C8 chains explored here); due to the high packing density of amphiphiles within the lamellae, lamellar phases generally are seen at higher concentrations for comparable hydrocarbon surfactants[26,27]. This behaviour is rationalised by the bulky and rigid nature of the fluorocarbon chains, leading them to favour low curvature interfaces such as lamellar sheets, as described by the principle of packing parameter[28].

Conversely, analogous hydrocarbon systems comprising sodium octanoate and either octan-1-ol or decan-1-ol show extremely rich phase behaviour, forming a variety of mesophases including lamellar, hexagonal, reverse hexagonal and rod-like structures[26,27,29]. The likely reason for the difference in structural behaviours is that the solubility of the components is much greater for the hydrocarbon system. This is characterised by the fact that the critical micelle concentration of sodium octanoate at *ca.* 300 mM[30] is nearly 10 times greater than that of sodium perfluorooctanoate at 30-36 mM[24,25].

Small-angle neutron scattering

Small angle neutron scattering was performed to characterise the transition from micellar to lamellar phases for the NaPFO/PFOH system, and also to probe the structural characteristics of the stable lamellar region. The scattering spectra for samples of NaPFO with no PFOH and small amounts of PFOH are shown in Fig. 2. The lowest trace (H28) is for a 5 wt% solution of NaPFO. In line with literature reports[14,24], the NaPFO has formed highly charged spherical micelles. Because the contrast between the NaPFO micelles and D_2O is actually quite low ($\rho_{NaPFO} = 3.8 \times 10^{10}$ cm^{-2}, $\rho_{D_2O} = 6.4 \times 10^{10}$ cm^{-2}), the intensity of this scattering from these micelles is comparatively weak. This sample was fit as described in the methods section, assuming a simple spherical form factor with a Schulz-type polydispersity function and a Hayter-Penfold charged sphere structure factor to account for the interaction between the charged micelles. Sample compositions and key fitted parameters from SANS measurements are presented in Table 1.

When only a tiny amount (0.1 wt%, sample N4) of PFOH is added to these NaPFO micelles, a structural change is evident. The scattering peak shifts to lower q, indicating a slight increase in micelle radius, and the beginnings of a sharper peak emerge at $q \approx 0.5$. We interpret this as a small amount of coexistent lamellar phase that is dispered throughout the sample. The viscosity appears to prevent macroscopic phase separation of the micellar and lamellar phases. When 0.2 wt% PFOH is added (sample N5), the nascent 'lamellar' peak increases in intensity, and scattering at low q with a characteristic q^{-4} dependency is seen, often interpreted as a critical 'surface scatter' from the faces of large structures such as lamellar sheets. When the ratio of PFOH:NaPFO (alcohol:surfactant) is increased yet further, a very different

Table 1 Sample compositions and fitted parameters from modelling of SANS experimental data, organised by sample name (Spl). Phase identities (Phs) were confirmed by polarising light microscopy and SANS spectra and volume fractions Φ, of dispersed material (NaPFO+PFOH) were calculated from molar volumes. Fitted parameters are the inter-lamellar spacing d, Caillé parameter η_{cp}, bilayer thickness δ, micellar radius r_{mic} and the area per headgroup, A_{hg}. Representative uncertainties are $d, \delta, r_{mic} \pm 0.3$ nm, $\eta \pm 0.02$ and $A_{hg} \pm 0.06$.

Spl	Phs	Composition (mass frac.)			Φ	d	η_{cp}	δ	r_{mic}	A_{hg}
		H_2O[a]	NaPFO	PFOH		nm		nm	nm	nm^2
H28	L_1	0.950	0.050	-	0.024	-	-	-	1.4	0.79[b]
H31	L_α	0.960	0.020	0.020	0.022	40.0[c]	-	-	-	-
H32	L_α	0.930	0.020	0.050	0.041	31.5	0.30	2.5	-	0.29
H33	$L_1 + L_\alpha$	0.930	0.050	0.020	0.036	15.2	0.53	1.9[d]	-	-
H34	$L_1 + L_\alpha$	0.900	0.050	0.050	0.056	-	-	-	-	-
H35	L_α	0.850	0.050	0.100	0.089	21.7	0.20	2.3	-	0.31
H37	L_α	0.800	0.100	0.100	0.117	17.0	0.14	2.1	-	0.33
H38	L_α	0.700	0.100	0.200	0.192	12.0	0.09	2.1	-	0.34
N1	L_α	0.780	0.110	0.110	0.130	16.1	0.11	2.3	-	0.31
N2	L_α	0.850	0.090	0.060	0.084	21.2	0.55	2.0	-	0.35
N3	L_α	0.880	0.040	0.080	0.070	25.8	0.13	2.4	-	0.30
N4	$L_1 + L_\alpha$	0.949	0.050	0.001	0.024	-	-	-	1.7	-
N5	$L_1 + L_\alpha$	0.948	0.050	0.002	0.025	-	-	-	1.7	-
N6	$L_1 + L_\alpha$	0.945	0.050	0.005	0.027	14.4	0.31	1.8	-	-
N7	$L_1 + L_\alpha$	0.931	0.049	0.020	0.036	13.9	0.27	1.7	-	-
N8	L_α	0.913	0.048	0.038	0.047	23.0	0.80	2.2	-	0.32
N16	L_α	0.930	0.035	0.035	0.038	-	-	-	-	-
N19	L_α	0.830	0.071	0.099	0.100	-	-	-	-	-

[a] Molar equivalent amounts of D_2O were used to prepare SANS samples.

[b] Calculated using aggregation number from Berr *et al.*[24]

[c] Approximated from $d = 2\pi/q_b$, where q_b is the position of the diffuse Bragg peak

[d] Refer to main text for a discussion of fitted parameters for mixed systems.

structure is observed (sample H31, 2 wt% NaPFO+2 wt% PFOH). The scattering from this sample is much more characteristic of a very poorly defined lamellar phase. If we assume that the left-most 'peak' is the characteristic Bragg diffraction, then the inter-lamellar spacing of this phase would be *ca.* 40 nm. It is possible that this structure is more akin to a 'perforated' lamellar phase, explaining the diffuse, double-humped peak[31], although for this dilute phase, the scattering peaks are not sufficiently resolved to be confident of this. Sens and Turner elegantly demonstrated that the effect if 'inclusions' into lamellar bilayers has the effect of broadening the Bragg peaks[32], and so the rather diffuse, broad peaks resulting from the combination of micelles and lamellar sheets seen here could be explained using this rationale.

For the samples that show lamellar/micellar coexistence, the scattering should technically be fitted as a linear combination of the intensity of the scattering from a known volume of micellar phase and lamellar phase. However, because the samples do not macroscopically phase separate due to kinetic trapping, the ratio of the two phases is not easily determined. By comparison of the scattering from a pure lamellar phase (e.g. N3, Fig. 3) with micellar scattering (H28, Fig. 2) it is seen that the intensity of scattering from the lamellar phase is ≈ 2 orders of magnitude greater than that from micelles. This suggests that any contribution from micellar scattering would be minor in the phase coexistence region. We test this supposition by comparing the separate and additive scattering from micellar and lamellar phases (assuming a simple additive relationship) – see Supplementary Information – and find that the Bragg peak and Caillé value for the lamellar scattering are essentially unaffected by the presence of the micellar phase. The δ value, which is influenced by the higher-q scattering where overall intensity is much lower would appear to be affected by up to $\pm 10\%$ and so δ values in Table 1 for samples H33, N6 and N7 should be interpreted with some caution.

The area per headgroup calcuated from the SANS data also supports the hypothesis that intercalation of the alcohol monomers between the surfactants induces the change in curvature from micelle to lamellar. The calculated area per headgroup for NaPFO in micelles at 0.05 wt% (0.1 mol dm^{-3}) is 0.79 nm^2. At this concentration, the micelles are rather highly charged (average aggregation number 26.5 and charges/micelle 17.2, giving an effective dissociation ratio of 65%)[24]. This area is quite large for both geometric and electrostatic reasons when compared to the minimum area per headgroup for NaPFO at the air-water interface of ≈ 0.3 nm^2, as determined by López-Fontán *et al.*[25]. Conversely, the area per headgroup calculated geometrically from fitted SANS parameters for the lamellar phases containing both NaPFO and PFOH is on the order 0.3-0.35 nm^2, and is quite insensitive to interfacial composition. Clearly these values do not distinguish between the surfactant and alcohol, and thus are an average based on the density of the composite lamellae. Nonetheless, the area is clearly significantly less than for NaPFO molecules in a micelle, reflecting closer packing that we posit is from reduced inter-headgroup repulsions.

A notable feature from the fitted lamellar SANS data is that the low-q region before the first Bragg peak tends to be fitted quite poorly, and some deviation is seen from the expected q^{-4} dependency of scattered intensity. This region generally represents the scattering from larger scale structures in samples, and is often most strongly affected by the structure factor, scattering from extended surfaces, poorly defined interfaces due to phase separation, etc.[33]. In the Nallet and Roux model used to fit the lamellar scattering here, this region corresponds to fluctuations in the extended bilayer surfaces. However, due to the other factors that may influence scattering in this region, the feature has proven to offer rather poor fits to the low-q scattering from a range of lamellar phases[34–36], although the reason for this is not entirely clear. It may suggest a departure from the ideal model of the bilayer due to perforation, inclusions, *etc.*

For certain systems, it is more appropriate to use a version of the Nallet and Roux model that accounts for multiple scattering steps corresponding to surfactant head- and tail-groups. In such a case, each bilayer would modelled as consisting of a central 'slab' of fluorocarbon chains with a layer of headgroups on each side. For the materials studied here, we find that this analysis would not be possible, due to insufficient contrast between the highly hydrated surfactant headgroups and the continuous solvent (D_2O). Such analysis would likely be possible for SAXS measurements of the same systems, where greater resolution of these features would be obtained due to the higher contrast between headgroups and solvent.

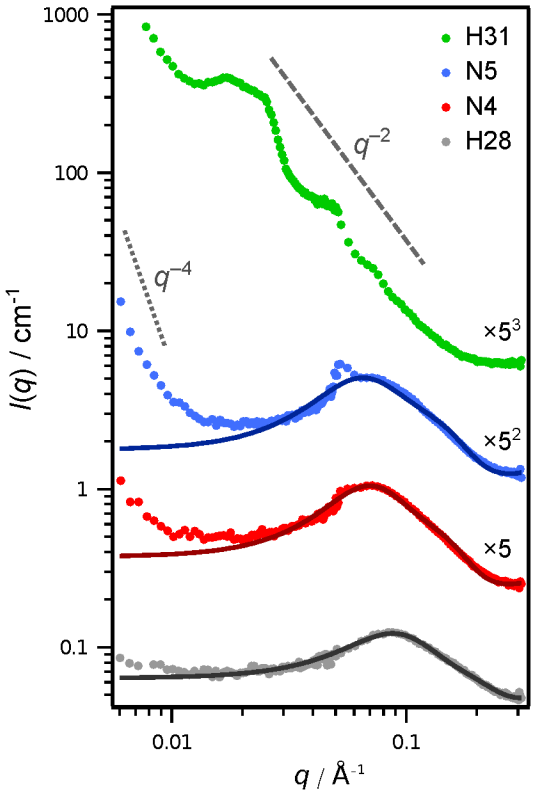

Fig. 2 SANS data and model fits for micellar and transitional phases of NaPFO+PFOH, plotted as the normalised intensity, $I(q)$ as a function of the scattering vector, q. Coloured symbols are experimental SANS data and solid lines are fits generated as described in the text. Plots are vertically offset as noted for clarity of presentation, and the dotted and dashed lines show q^{-4} and q^{-2} dependencies for comparitive purposes.

At increasing volume fractions of surfactant and co-surfactant ($0.07 \leq \Phi \leq 0.19$), well-developed lamellar phases formed, with their scattering shown in Fig. 3. As indicated by the lack of flow on inversion for these samples (Fig. 1) they had very high viscosities, and appeared to be effectively 'gelled' (*i.e.* immobile on inversion, and retaining their shape when sheared by a pipette). Perhaps most notable from their scattering spectra is the level of order seen within these lamellar phases. For many samples, 4th and even 5th order peaks are visible in the scattering, indicating high levels of local order. In comparison, typical lamellar phases stabilised by hydrocarbon surfactants show one or two peaks at comparable volume fractions[36]. Once again, this can be rationalised by the structure of the surfactant and alcohol. As both are relatively short and rigid, they tend to favour very planar interfaces

that are comparatively rigid. The high interfacial tension of the perfluorocarbon-water interface demonstrates the greater hydrophobicity of fluorocarbons when compared to hydrocarbons, and thus a strong hydrophobic attraction can be expected to act between neighbouring chains in the lamellar sheets.

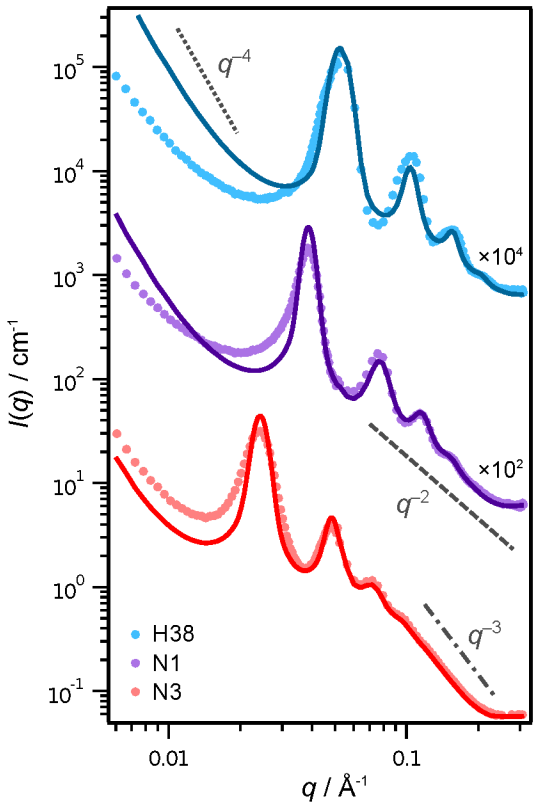

Fig. 3 SANS data with model fits from fluorinated lamellar phases of NaPFO+PFOH. Coloured symbols are experimental SANS data and solid lines are fits generated as described in the text. Plots are vertically offset as noted for clarity of presentation, and the dotted, dashed and dot-dashed lines show q^{-4}, q^{-2} and q^{-3} dependencies for comparitive purposes.

The Caillé parameter is a useful measure of the rigidity of the lamellar membranes, with a low value indicating a high bending modulus, and low values indicating flexible bilayers. It can be seen from the values in Table 1, obtained from model fitting of the SANS data, that the Caillé values, η_{cp} for these systems vary widely with composition. The phases with the highest volume fractions of surfactant and alcohol (H38 and N1) also have the lowest Caillé values, suggesting that packing is influential in the rigidity of the membranes, with denser packing favouring more rigid bilayers. Conversely, the lower volume fraction samples tend to have high Caillé values, indicating flaccid, flexible membranes. Beyond this extreme, there is however only a tenuous correlation between the Caillé value and other parameters.

Finally from the SANS fitting we can conclude that there is little difference in the bilayer thickness between all lamellar samples. As the internal surface of the bilayer comprises the fluorocarbon chains, we would expect very little variation between samples with different ratios of the structurally similar tailgroups of the surfactant and alcohol.

A further complication arises in the scattering data due to the very high viscosities of some of the higher volume fraction lamellar phases. Figure 4 shows the 2D raw scattering patterns obtained on the SANS detector, demonstrating a moderate degree of radial anisotropy for samples H37 and H38. This suggests that the samples retained some level of alignment in the scattering cell, probably induced as they were pipetted in using standard glass Pasteur pipettes. We neglected the effect of this minor alignment in radially averaging the samples, as the level of anisotropy was not sufficient to significantly detract from qualitative modelling of the data. However, it is another strong indicator of the long relaxation times of the higher volume fraction samples.

As expected, the bilayer spacing decreases with increasing total volume fraction ϕ of additives (surfactant+alcohol) as shown in Fig. 4. From a pure volume exclusion argument, it would be expected that the relationship between ϕ and d would be such that $d \propto 1/\phi$, as demonstrated by Strey *et al.*[37]. Thus if the volume fraction of bilayers doubles, they must on average be twice as close together. From the inset to Fig. 4, it is clear that this is broadly the case for low $1/\phi$ values, *i.e.* for densely packed systems. Even then, the line of best fit through most dense 6 samples does not tend directly towards the origin, suggesting some level of non-ideality in the system. At lower volume fractions, there is a much more significant departure from this dependence. When viewed on d *vs* ϕ axes, a more clear relationship is visible, wherein the low volume fraction systems are split between those that broadly obey the trend (with large lamellar spacings) and those with apparently aberrantly low inter-lamellar spacings. The samples with apparently errant low spacings are highlighted in each panel by the shaded box, and it is these compositions that we posit are in fact exhibiting lamellar-micellar coexistence, wherein a densely packed lamellar phase coexists with a dilute lamellar phase. Due to their high viscosity, they are kinetically trapped, and cannot resolve into two macroscopic phases. As the scattering from the micelles is so weak in comparison to the intense, structured scatter from the lamellar phase, it is very difficult to detect in the SANS spectrum. To confirm this, a diffusion measurement (such as fluorescence correlation spectroscopy) could be performed, as it should clearly show two

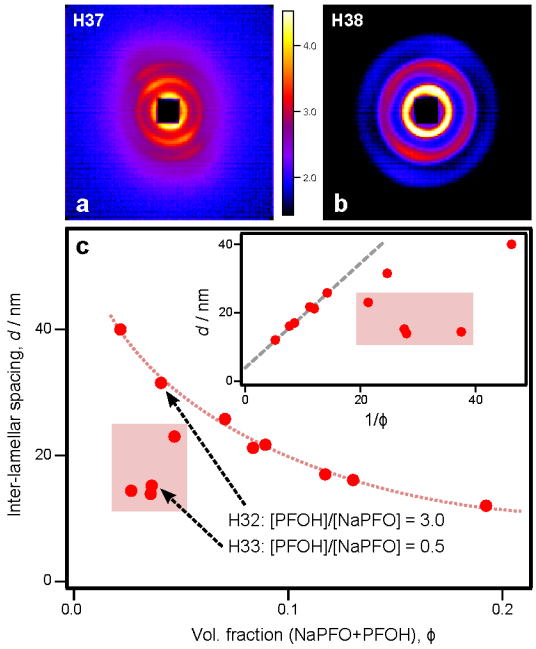

Fig. 4 a), b) Raw 2D SANS detector patterns for two representative lamellar phases showing some degree of aniostropic scattering. The images are 128×128 pixels, representing the elements of the physical ^{3}He SANS detector. The colours represent the scaled number of neutrons incident at each 'pixel'. c) The relationship between the inter-lamellar spacing and the volume fraction of bilayer material (surfactant+alcohol). The dotted line is drawn as a guide to the eye. The inset shows the same data plotted against $1/\phi$, and the dashed line is a linear fit to the six highest volume fraction samples. The shaded boxes highlight samples that exhibit lamellar+micellar phase coexistence.

diffusion coefficients for the lamellar and micellar structures.

Rheology

The macroscopic bulk rheological properties of the different samples reflect their internal microstructure[19]. Small angle oscillatory tests were performed on samples N1 (11 wt% NaPFO and 11 wt% PFOH), N16 (3.5 wt% NaPFO and 3.5 wt% PFOH), H32 (2 wt% NaPFO and 5 wt% PFOH) and N19 (7.1 wt% NaPFO and 9.9 wt% PFOH). Initial stress sweep tests were performed at 0.1 Hz and 10 Hz in order to determine the linear viscoelastic region for each sample. Based on this, subsequent frequency sweeps were performed at 0.5 Pa, where the materials tested were all linear. The elastic or storage modulus (G') and the viscous or loss modulus (G'') are plotted as a function of oscillation frequency in Fig. 5a. The limits of the rheometer and the geometry meant that the frequency range was material dependent. For example, at high frequencies, secondary flows caused G' to decrease from the plateau, which was not feasible. The maximum frequency was 1 to 10 s^{-1}. At low frequencies, the time required for each oscillation meant artefacts due to evaporation were possible. The minimum frequency was 0.01 to 0.1 s^{-1}.

The four samples showed large variation in the magnitudes of their moduli and the frequencies at which G' was greater than G'' (signifying solid-like behaviour) or G' was less than G'' (fluid-like behaviour). At low enough frequencies, the samples were in the viscous or terminal region where $G'' > G'$, except for H32. The moduli were equal ($G' = G''$) at the cross-over frequency, ω_c. The longest relaxation time, τ, is usually taken as the reciprocal of the cross-over frequency. Beyond the cross-over frequency, the samples were in the rubbery or plateau region where $G' > G''$ and elastic behaviour dominated. This behaviour is illustrated well by H32, showing constant and large G' for nearly all frequencies. In this region, G' may reach a peak and G'' may begin to fall and even begin to increase again[38].

The oscillatory results for N19 and H32 did not show a cross-over frequency. The single-mode Maxwell model was used to extrapolate the data to estimate a value for the cross-over. A Maxwell fluid is visualised as an elastic spring in series with a viscous dashpot and shows quadratic G' and linear G'' dependencies with frequency:

$$G' = \frac{G(\omega\tau)^2}{1+(\omega\tau)^2} \quad (9) \qquad G'' = \frac{\eta\omega}{1+(\omega\tau)^2} \quad (10)$$

G is the characteristic modulus for the Maxwell fluid and twice the modulus at the cross-over frequency. η is the fluid viscosity and is the product of G_c and τ. The experimental (N1 and N16) and extrapolated (N19 and H32) cross-over frequencies and moduli are given in Table 2.

Table 2 Cross-over frequency, relaxation time and cross-over modulus from oscillatory rheology tests. τ is the reciprocal of ω_c. The values for N19 and H32 are extrapolated using a Maxwell model.

Sample	ω_c / s^{-1}	τ / s	G_c / Pa
N1	0.23	4.3	26
N16	0.38	2.6	15
N19	0.0079	127	475
H32	0.0011	917	458

The NaPFO-PFOH samples were of course more complicated than the simple Maxwell model, and would be expected to show a spectrum of relaxation times. The use of the Maxwell

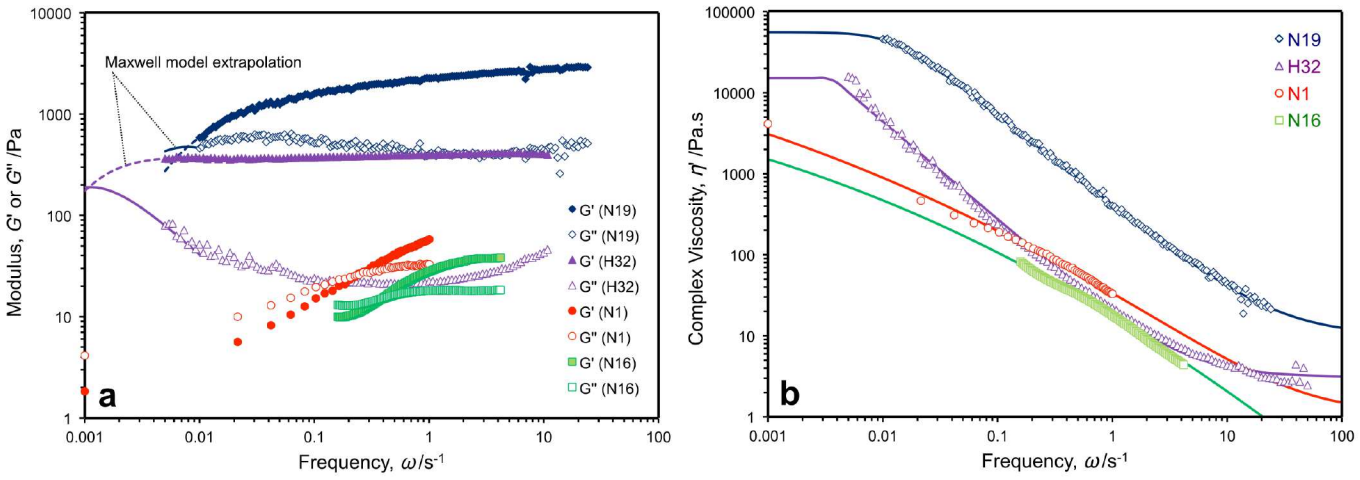

Fig. 5 a: Elastic (G', filled symbols) and viscous (G'', open symbols) moduli of four samples (N1, N16, N19 and H32). The cross-over frequency is the reciprocal of the longest relaxation time τ. The dashed and solid lines represent Maxwell model extrapolations for N19 and H32. **b**: Complex viscosity of samples N1, N16, N19 and H32 calculated from $\eta' = G''/\omega$. The results have been fitted with a Carreau fluid model (the fitted values given in Table 3).

model across all frequencies is certainly not justified, and it is used here to simply extrapolate the data to facilitate qualitative comparisons.

Samples N16 and N1 both contained a ratio of 1:1 [PFOH]/[NaPFO] but differing water contents (93% and 78% respectively). The variation in modulus and relaxation time followed the expected concentration dependency with the lowest water content showing the largest modulus and longest relaxation time. Samples N19 and H32 had higher concentration ratios of 1.4 and 2.5 respectively, and N19 had a water content of 83% (similar to N1 at 78%) compared to 93% for H32 (the same as N16). The higher moduli and longer relaxation times for N19 and H32 compared to the 1:1 samples show clearly that increased relative amounts of PFOH led to significant changes in the rheological response, likely related to differences in the microstructure as shown by SANS.

The complex viscosity, calculated from $\eta' = G''/\omega$, is shown in Figure 5b. The samples showed shear thinning behaviour across the frequency range, behaviour that is well known for dilute lamellar phases.[19] The shear thinning behaviour of such systems is often ascribed to either alignment or breakdown of the lamellar structure due to shear.[39] N19 appeared to approach a limiting zero shear viscosity η_∞, whilst H32 approached a limiting high shear viscosity η_0, suggesting the use of an oscillatory version of a single-relaxation Carreau fluid model[40] to fit the data:

$$\frac{\eta' - \eta_\infty}{\eta_0 - \eta_\infty} = (1 + (\lambda\omega)^a)^{\frac{n-1}{a}} \qquad (11)$$

In Eq. 11, λ is the Carreau relaxation time (compared with the Maxwell relaxation time τ), a is a fitting parameter and n is the power index. Since the data was geometrically distributed, the model was fitted to $\log_e \eta'$ versus $\log_e \omega$ to minimise skewing at large frequency. The model was fitted with the constraints that a and λ were positive. The fitted parameters are given in Table3.

Table 3 Carreau model fitting parameters for complex viscosity

Sample	η_0/ Pa·s	η_∞/ Pa·s	λ / s	a	n
N1	193,000	1.12	4.99	0.142	-0.516
N16	33,700	0	8.41	0.172	-0.456
N19	57,600	10.2	83.3	2.54	-0.115
H32	15,550	3.13	277	34.4	-0.210

The regression was fairly insensitive to η_0 and η_∞ when the data did not deviate significantly from power-law behaviour, and so the extrapolated values of these parameters for N1 and N16 are imprecise and poorly defined. Encouragingly, the Carreau relaxation time was of similar magnitude to the Maxwell relaxation time and the two parameters showed the

same trend between the samples.

There was no shear thickening or dramatic changes in the shear-thinning behaviour observed, suggesting that shearing the samples did not induce phase changes or secondary structures. We therefore posit that these phases would make effective thick film lubricants[41], due to the combination of their high viscosity at rest and shear-thinning characteristics.

Templating

Initially, templating was attempted using a stirred process whereby 0.05 g TEOS was added to a 1 g of NaPFO/PFOH/water lamellar phase (sample N19, composition in Table 1) and left stirring for 14 hours. Although the material generated using this method was birefringent, suggesting that a level of structuring was obtained, AFM imaging showed that a large amount amorphous silica had been produced, along with particles on the order of 10-100 nm.

Thus a new protocol was developed wherein the TEOS and lamellar phase were mixed initially by stirring (for 1 minute) followed by an unstirred aging period of 14 hours. The resultant phase was then freeze dried and calcined in a furnace in ambient air for 12 hours at 600°C. This method generated silica that showed high levels of birefringence when examined with polarising light microscopy; AFM imaging confirmed that the lamellar strucure of the soft matter template had indeed be replicated. Sectional analysis of AFM images revealed that the lamellae themselves are very thin (*ca.* 1 nm) and the spacing between lamellae was on the order of 10 nm, comparable to that in the parent lamellar phase.

Silica materials have been templated from various self-assembled surfactant phases using TEOS, and thus a number of researchers have sought to understand the mechanism by which silica forms under such conditions. It has been shown that the hydrophobic TEOS molecules tend to partition mostly to the oily phase in a two phase system, which may be the internal space of surfactant aggregates such as micelles/microemulsion droplets, or a bulk (continuous) oil phase when water-in-oil microemulsions are used as the supporting medium. By diffusing to the surfactant-water interface, the TEOS molecules can then be hydrolysed by water, forming silanol groups and releasing ethanol. The hydrolysed silica species then condense to give mineralised silica within the water spaces of the self-assembled phase.

In our experiments, it is assumed that the TEOS initially locates within the hydrophobic fluorocarbon space inside the lamellae composed of the surfactant and alcohol chains. Diffusion to the surfactant headgroups at the water interface would then permit hydrolysis followed by mineralisation. The question of the role of the excluded ethanol that is produced during this process in the phase behaviour of the system has been explored for microemulsions, where it was found to in some cases cause macroscopic phase separation. Here, the relatively small amount generated (44 mg) did not appear to alter phase behaviour, and adding the same amount to a 'blank' lamellar sample with the same NaPFO/PFOH composition caused no discernable change in properties.

Powder diffraction measurements were used to ensure that the silica itself was non-crystalline and showed no significant ordering below the ≈10 nm spacing between lamellae (Fig. 6); this was indeed the case. These measurements also suggested that no crystalline NaPFO was presented in the post-calcination silica. Ideally we would confirm the structure of the silica by SAXS measurements, but time did not permit this. By measuring the powder diffraction spectrum of pure NaPFO, we were also able to confirm that none of the template material remained after drying and calcining. Interestingly, some peaks are seen in the spectrum of the liquid crystal template, suggesting that some order on very small scales is observed. The peaks representing spacings of *ca.* 10 and 15 Å may result from the proximity of the fluorocarbon chains on neighbouring molecules in the lamellar sheets, although a more detailed and systematic study of the wide-angle scattering behaviour of these system is beyond the scope of the present work. Although full characterisation of the templated material by small-angle X-ray scattering and electron microscopy is desirable, it is clear from Fig. 6 that the silica shows structural characteristics suggesting replication of the lamellar template.

Clearly much work remains to optimise the templating procedure, with the ultimate goal of forming complete monoliths of silica that are oriented by shear to align the lamellar director. However, the proof of principle shown here demonstrates that fluorinated lamellar phases make excellent templates for the generation of highly-ordered silica, and this process can now be explored further. Such silica is not only of interest due to its high surface area to mass ratio, but also because the lamellae induce highly aniostropic fluid flow.

Conclusion

Mixtures of perfluorooctanoic acid (NaPFO) and the partially fluorinated alcohol PFOH readily form lamellar phases of high viscosity. Like many lamellar systems, these liquid crystals are highly shear thinning, and exhibit behaviour that can be characterised rheologically in terms of their elastic and viscous moduli. By using small-angle neutron scattering, we

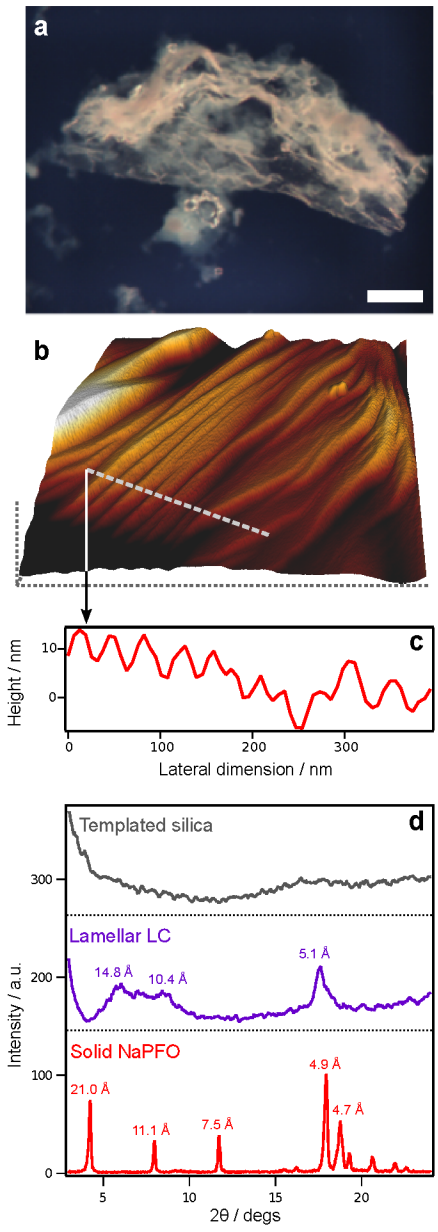

Fig. 6 Silica templated from fluorinated lamellar phase N19. a) polarising light microscopy image. The scale bar is 200 um. b) AFM topographic image of a typical section of the sample surface showing lamellar 'terraces'. The 'box' dimensions are 800×800×40 nm. c) Sectional profile from the image in (b) showing the characteristic inter-lamellar 'steps' on the surface of the material. d) Powder diffraction spectra for solid NaPFO, the parent fluorinated lamellar phase and the templated silica.

were able to characterise the internal nanostructure of these liquid crystals. Through adding a silicate precursor, these fluorinated liquid crystals were shown to be an effective template for highly-ordered, high surface area inorganic materials.

The lamellar phases obtained were found to exhibit a high degree of local order when compared to analagous hydrocarbon systems. This behaviour is rationalised by considering the unique nature of fluorocarbon compounds. The highly polar C-F bond and larger van der Waals radius compared to hydrogen results in a significantly bulkier and more rigid carbon chain, and this is what drives the apparent preference for low-curvature self-assembled systems.

As well as showing potential as an effective lubricant due to their shear-thinning nature, the fluorinated liquid crystals were also found to be a useful substrate for building high surface area silica structures. This lamellar-templated silica structure is of great interest, with potential applications in filtration as well as the fields of catalysis and gas adsorption in common with other microporous silica materials. The high degree of local order imparted specifically by fluorocarbons may aid in the production of more ordered silicates for these applications.

The primary reasons for the unique phase behaviour and properties seen for these fluorcarbon phases appear to be a balance between head-group interactions and the bulky fluorocarbon chains, and the extreme hydrophobicity of the fluorocarbons themselves. It has been demonstrated that similar properties can be achieved in some systems by incorporating high levels of branching in hydrocarbon alkyl groups[42] to give low dispersive energy chains. This approach may now be pursued in order to also mimic the rigid, bulky nature of the fluorocarbon and thus obtain similar phase characteristics.

Acknowledgement

The subcommittee and the ILL are thanked for the allocation of beam time at the ILL. We acknowledge the support of the Bragg Institute, Australian Nuclear Science and Technology Organisation, in providing neutron research facilities used in this work. T. K. acknowledges funding from The University of Melbourne through a Melbourne International Research Scholarship. Infrastructure support for the rheology measurements was provided by the Particulate Fluids Processing Centre, a Special Research Centre of the Australian Research Council. We are indebted to Brendan Wilkinson and Bruce Dobney for their assistance in drying and calcining the silica samples.

References

1 R. C. Buck, P. M. Murphy and M. Pabon, in *Polyfluorinated Chemicals and Transformation Products*, ed. T. P. Knepper and F. T. Lange, Springer, New York, 2012, ch. Chemistry, Properties, and Uses of Commercial Fluorinated Surfactants.

2 R. F. Tabor, C. Wu, F. Grieser, R. R. Dagastine and D. Y. C. Chan, *J. Phys. Chem. Lett*, 2013, **4**, 3872–3877.

3 M. Almgren, V. M. Garamus, L. Nordstierna, J. Luc-Blin and M.-J. Stebe, *Langmuir*, 2010, **26**, 5355–5363.

4 S. E. Rogers, J. Eastoe, L. Hudson, S. Gold, R. K. Heenan and I. Grillo, *J. Colloid Interface Sci.*, 2009, **330**, 437–442.

5 M. Hollamby, J. Eastoe, K. J. Mutch, S. E. Rogers and R. K. Heenan, *Soft Matter*, 2010, **6**, 971–976.

6 R. Fowler, W. Buford III, J. Hamilton Jr., R. Sweet, C. Weber, J. Kasper and I. Litant, *Ind. Eng. Chem.*, 1947, **39**, 292–298.

7 M. M. MacDonald, M. J. A. Dinglasan-Panlilio, S. A. Mabury, K. R. Solomon and P. K. Sibley, *Env. Sci. Tech.*, 2007, **41**, 7159–7163.

8 H. R. Ropers and M.-J. Stebe, *Phys. Chem. Chem. Phys.*, 2001, **3**, 4029–4036.

9 P. Kekicheff and G. J. T. Tiddy, *J. Phys. Chem.*, 1989, **93**, 2520–2526.

10 H. T. Jung, B. Coldren, J. A. Zasadzinski, D. J. Iampietro and E. W. Kaler, *Proc. Natl. Acad. Sci. U.S.A.*, 2001, **98**, 1353–1357.

11 J. T. Mang, S. Kumar and B. Hammouda, *Europhys. Lett.*, 1994, **28**, 489–494.

12 S. Ristori, G. Gebel and G. Martini, *Coll. Surf. A*, 1993, **80**, 113–120.

13 Z.-J. Yu and D. Neuman, *Langmuir*, 1994, **10**, 377–380.

14 E. Caponetti, D. Chillura Martino, M. A. Floriano and R. Triolo, *Langmuir*, 1993, **9**, 1193–1200.

15 M. Benrraou, B. L. Bales and R. Zana, *J. Phys. Chem. B*, 2003, **107**, 13432–13440.

16 J. Eastoe, G. Fragneto, B. H. Robinson, T. F. Towey, R. K. Heenan and F. J. Leng, *J. Chem. Soc., Faraday Trans.*, 1992, **88**, 461–471.

17 S. Mele, B. W. Ninham and M. Monduzzi, *J. Phys. Chem. B*, 2004, **108**, 17751–17759.

18 S. Fuller, Y. Li, G. J. T. Tiddy and E. Wyn-Jones, *Langmuir*, 1996, **11**, 1980–1983.

19 M. G. Berni, C. J. Lawrence and D. Machin, *Adv. Colloid Interface Sci.*, 2002, **98**, 217–243.

20 P. Bartlett and R. H. Ottewill, *J. Chem. Phys.*, 1992, **96**, 3306.

21 J. B. Hayter and J. Penfold, *Mol. Phys.*, 1981, **42**, 109–118.

22 F. Nallet, R. Laversanne and D. Roux, *J. Phys. II France*, 1993, **3**, 487–502.

23 A. Caille, *C. R. Hebd. Acad. Sci. Paris B*, 1972, **274**, 891–893.

24 S. S. Berr and R. R. M. Jones, *J. Phys. Chem.*, 1989, **93**, 2555–2558.

25 J. L. Lopez-Fontan, F. Sarmiento and P. C. Schulz, *Colloid. Polym. Sci.*, 2005, **283**, 862–871.

26 G. J. T. Tiddy, *J. Chem. Soc., Faraday Trans. 1*, 1972, **68**, 369–380.

27 C. J. James and J. F. Heathcock, *J. Chem. Soc., Faraday Trans. 1*, 1981, **77**, 2857–2865.

28 J. N. Israelachvili, D. J. Mitchell and B. W. Ninham, *J. Chem. Soc., Faraday Trans. 2*, 1976, **72**, 1525–1568.

29 Y. Sasanuma, F. Nishimura, H. Wakabayashi and A. Suzuki, *Langmuir*, 2004, **20**, 665–672.

30 F. E. Stanley, A. M. Warner, E. Schneiderman and A. M. Stalcup, *J Chromatogr. A*, 2009, **1216**, 8431–8434.

31 C. N. Lam and B. D. Olsen, *Soft Matter*, 2013, **9**, 2393–2402.

32 P. Sens and M. S. Turner, *Eur. Phys. J. E*, 2001, **4**, 115–120.

33 *Neutron, X-rays and Light. Scattering Methods Applied to Soft Condensed Matter*, ed. T. Zemb and P. Lindner, North–Holland, Amsterdam, 2002.

34 F. Nettesheim, C. B. Muller, U. Olsson and W. Richtering, *Coll. Poly. Sci.*, 2004, **282**, 918–926.

35 F. Castro-Roman, L. Porcar, G. Porte and C. Ligoure, *Eur. Phys. J. E*, 2005, **18**, 259–272.

36 R. F. Tabor, M. I. Zaveer, R. R. Dagastine, I. Grillo and C. J. Garvey, *Langmuir*, 2013, **29**, 3575–3582.

37 R. Strey, R. Schomacker, D. Roux, F. Nallet and U. Olsson, *J. Chem. Soc., Faraday Trans.*, 1990, **86**, 2253–2261.

38 H. A. Barnes, *A Handbook of Elementary Rheology*, University of Wales Institute of Non-Newtonian Fluid Mechanics, Aberystwyth, 2000.

39 Y. Shen, H. Hoffmann, L. Jiang, H. Lin, J. Hao and L. Yang, *Colloid Polym. Sci.*, 2014, **292**, 67–75.

40 P. J. Carreau, *Trans. Soc. Rheology*, 1972, **16**, 99–127.

41 A. W. Sisko, *Ind. Eng. Chem.*, 1958, **50**, 1789–1792.

42 M. Hollamby, K. Trickett, A. Mohamed, S. Cummings, R. F. Tabor, O. Myakonkaya, S. Gold, S. E. Rogers, R. K. Heenan and J. Eastoe, *Angew. Chem. Int. Ed.*, 2009, **48**, 4995–4998.

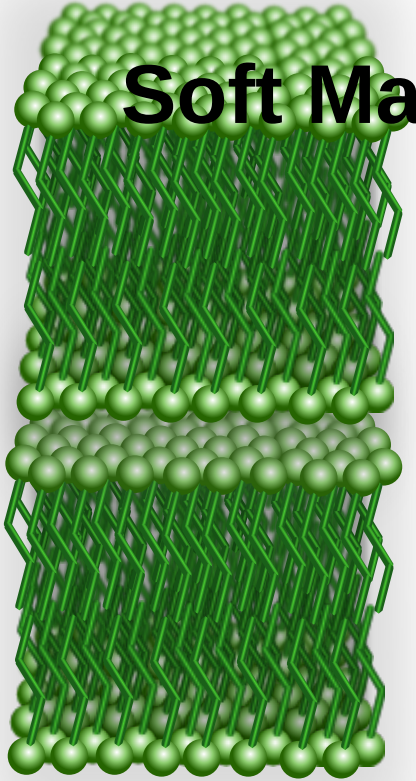

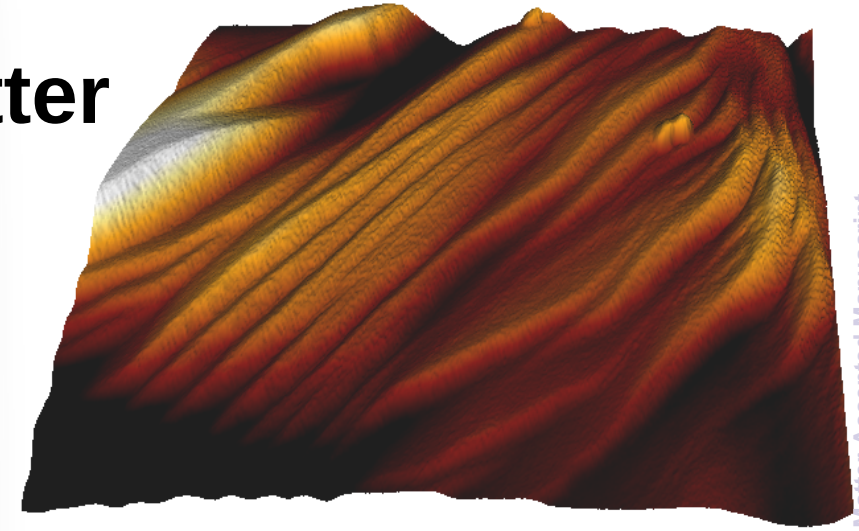

Lamellar templated silica